Solid State Ionics 422 (2025) 116803

Contents lists available at ScienceDirect

Solid State Ionics

journal homepage: www.elsevier.com/locate/ssi

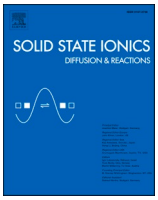

$Ca_{1-x}Sr_xMnO_{3-\delta}$ granules, pellets, foams: Influence of fabrication conditions and microstructure on oxidation kinetics

Lena Klaas [a,b,*], Asmaa Eltayeb [a], Dorottya Kriechbaumer [a], Martin Roeb [a], Christian Sattler [a,b]

[a] Deutsches Zentrum für Luft- und Raumfahrt – DLR, German Aerospace Center, Institute of Future Fuels, Linder Höhe, Cologne 51147, Germany
[b] RWTH Aachen, Faculty of Mechanical Engineering, Chair for Solar Fuel Production, Aachen 52062, Germany

ARTICLE INFO

Keywords:
Thermochemical cycles
Perovskites
Morphology
Microstructure
Oxidation kinetics

ABSTRACT

Microstructure and oxidation kinetics are closely intertwined factors that significantly influence the behavior of materials in oxidative environments. This relationship is of particular importance for redox materials such as $Ca_{1-x}Sr_xMnO_{3-\delta}$, where reversible oxygen ions exchange and oxidation state shifts are key to their functionality. In the first study, scanning electron microscope (SEM) was used to examine how varying Sr content affects the morphology and microstructure of $Ca_{1-x}Sr_xMnO_{3-\delta}$ powder compositions. The results indicate that increasing Sr content leads to smaller particle sizes and improved particle size homogeneity. Granules with Sr concentrations ranging from 0 % to 40 % exhibit notable changes in morphology. However, the microporosity and d50 vary slightly across the samples in a non-monotonic manner, with no clear trend emerging with respect to Sr concentration. The second study investigates how macrostructural forms, such as foams and pellets, impact oxidation kinetics in $Ca_{0.8}Sr_{0.2}MnO_{3-\delta}$. Parameters including particle size distribution of the raw material, overall microporosity, and structural characteristics of these macrostructures were analyzed for their effect on oxidation rates. Findings reveal that macrostructural configuration, alongside microstructural features like microporosity, significantly impacts oxidation kinetics. These studies collectively underscore the critical relationship between dopant concentration, microstructural characteristics, and structural morphology in determining the oxidative behavior of $Ca_{1-x}Sr_xMnO_{3-\delta}$, providing key insights into optimizing material performance in redox environments.

1. Introduction

Materials with the chemical formula $ABO_{3-\delta}$ are commonly referred to as perovskites. One fascinating characteristic of this class of materials is their ability to accommodate or release non-stoichiometric amounts of oxygen without undergoing significant phase transition. Although minor phase transitions from e.g. orthorhombic to cubic can be observed during these reductions. Goldyreva et al. [1]; Klaas et al. [2] The amount of oxygen in perovskites can be controlled by adjusting the temperature, the oxygen partial pressure or both, which makes them particularly interesting for various thermochemical applications. These applications include thermochemical oxygen pumping Agrafiotis et al. [3]; Bulfin et al. [4]; Pein et al. [5], air separation (AS) Yang et al. [6]; Vieten et al. [7]; Bush et al. [8]; Vieten et al. [9]; Ezbiri et al. [10]; Farr et al. [11], chemical looping partial oxidation of methane (CLPOM) Tang et al. [12], chemical looping combustion (CLC) Galinsky et al. [13]; Luongo et al. [14], CO_2- and H_2O-splitting (CDS/WS) Riaz et al. [15]; McDaniel et al. [16,17]; Emery et al. [18]; Kubicek et al. [19]; Qian et al. [20] and thermochemical heat storage (TCS) Babiniec et al. [21]; Imponenti et al. [22]; Mastronardo et al. [23]; Buck et al. [24]. In this context, materials based on $CaMnO_3$ compositions are especially considered for tasks involving the regulation of oxygen partial pressure in oxygen pumping and AS, Agrafiotis et al. [3]; Pein et al. [5]; Vieten et al. [25], various looping processes like CLPOM and CLC Galinsky et al. [13]; Luongo et al. [14], and TCS Imponenti et al. [22]; Mastronardo et al. [23]; Jin et al. [26].

This paper primarily focuses on $Ca_{1-x}Sr_xMnO_{3-\delta}$, an advantageous material due to its non-toxicity, consisting solely of elements that are abundant and cheap Gaultois et al. [27]. Previous studies Klaas et al. [2,28] have explored and discussed the impact of Sr content on the crystal structure, the thermodynamics and the kinetics of $Ca_{1-x}Sr_xMnO_{3-\delta}$. In particular, the thermodynamic and kinetic

* Corresponding author at: Deutsches Zentrum für Luft- und Raumfahrt - DLR / German Aerospace Center, Institute of Future Fuels, Linder Höhe, Cologne 51147, Germany.
E-mail address: Lena.Klaas@dlr.de (L. Klaas).

https://doi.org/10.1016/j.ssi.2025.116803
Received 22 March 2024; Received in revised form 30 January 2025; Accepted 30 January 2025
Available online 6 March 2025

properties are important for practical applications, as they significantly influence process parameters such as temperature and reduction-oxidation cycle length duration. However, these studies have not taken into account the influence of different macrostructures, such as foams and granules, which are particularly relevant for these applications.

This study aims to fill this gap by providing a detailed microstructural analysis of $Ca_{1-x}Sr_xMnO_{3-\delta}$ with varying Sr content, as well as assessing the impact of microstructural changes on oxidation kinetics, thereby advancing its potential for industrial applications. To accomplish this, the study initially investigates the influence of Sr content on the morphology of powders (**P**) and granules (**G**). In addition, the evolution of the specific surface area and porosity of the granules in response to the varying Sr content is examined.The Sr solubility limit in $Ca_{1-x}Sr_xMnO_{3-\delta}$ for a synthesis in air is close to $x = 0.45$. Majewski et al. [29]; Chmaissem et al. [30] Therefore, only samples up to a Sr-content of 40 % are analyzed to ensure sufficient sample stability and consistency. This decision allows for a safer margin within the established limits and helps avoid potential complications during synthesis. Finally, to extend these findings, the study examines the effects of particle size distribution of the raw material and, subsequently, microporosity of larger macrostructures, specifically foams and pellets, providing insight into how these parameters influence oxidation kinetics at larger scales.

2. Theoretical background

2.1. Fundamentals for the kinetic consideration

The kinetics of oxidation and reduction processes are crucial for material applications, since they govern the time required for these processes steps. Depending on the application, either slow or fast kinetics are of interest. Therefore, it's essential to study both oxidation and reduction reactions with respect to their kinetics. A previous study Klaas et al. [28] has already shown that the material exhibits rapid reduction kinetics. However, this paper focuses exclusively on the oxidation kinetics.

In this study, the isoconversional method for analyzing kinetics is applied, following the *ICTAC Kinetics Committee recommendations for performing kinetic computations on thermal analysis data* Vyazovkin et al. [31]. This method has been successfully applied in similar studies on perovskites Bulfin et al. [32,33]; Klaas et al. [28]; Capstick et al. [34]. This model is potentially limited when predicting the equilibrium non-stoichiometry in the steady state. The underlying assumption is that the process rates can be parameterized by the temperature T, the conversion extent X, and the oxygen concentration c_{O_2}:

$$\frac{dX}{dt} = k(T)f(X)h(c_{O_2}), \tag{1}$$

where $k(T)$ is the rate constant, $f(X)$ is a function of the conversion extent and $h(c_{O_2})$ is a function for the dependence on the oxygen concentration.

Here, the rate constant $k(T)$ is given by an Arrhenius equation:

$$k(T) = k_0 \cdot exp\left(-\frac{E_A}{RT}\right) \tag{2}$$

where k_0 is the pre-exponential factor, E_A is the effective activation energy, and R is the gas constant. An oxidation process consists of several individual steps: first, oxygen is adsorbed at the surface, followed by dissociation of the molecule at the surface. Second, oxygen reacts with an oxygen vacancy in a layer in proximity to the surface. Lastly, oxygen diffuses through the bulk. de Souza [35] With the experiments used, these individual steps cannot be separated. Therefore, the resulting activation energy is referred to as an effective activation energy.

The dependence on the oxygen concentration $h(c_{O_2})$ is given by $h(c_{O_2}) = c_{O_2}^n$. n is the order of the oxygen concentration dependence. An earlier study by *Klaas* et al. Klaas et al. [28] showed that the oxidation kinetics of $Ca_{1-x}Sr_xMnO_{3-\delta}$ is independent of the oxygen concentration and therefore, $n = 0$.

The isoconversional principle states that the reaction rate at a constant extent of conversion is solely a function of temperature Vyazovkin et al. [31]. The differential isoconversional method is applied based on this principle. For a fixed value of conversion extent X, all functions are inserted into eq. 1, which is then reformulated, and a logarithm is taken on both sides. This results in:

$$log\left(c_{O_2}{}^{-n}\left(\frac{dX}{dt}\right)_{X=\text{const.}}\right) = -\frac{E_A}{RT} + log\left(k_0 f(X)_{X=\text{const.}}\right). \tag{3}$$

A logarithmic plot of $c_{O_2}{}^{-n}\left(\frac{dX}{dt}\right)_{X=\text{const.}}$ vs. $\frac{10^3}{RT}$ yields a line, and fitting this line provides the activation energy as the slope (details in Section 3.5).

3. Experimental methods

3.1. Solid-state method

The required mass according to the desired final stoichiometry of the precursors, $CaCO_3$ (*Merck*), $SrCO_3$ (*VWR International GmbH*) and Mn_3O_4 (*ERACHEM*), each with purities higher than 98 %, were weighted. The materials were first wet-mixed to ensure high phase purity, to prevent the formation of undesired side phases, and to replicate consistent results. This wet-mixing process facilitates the homogenization of the feedstocks.

To achieve this, $SrCO_3$ was dispersed in isopropanol and continuously stirred using a stirring rod at 333 K. Once the powder had agglutinated, it was further refined by sieving it into the isopropanol. After approximately 15 min of mixing, $CaCO_3$ and Mn_3O_4 were added and continuously mixed for 24 h. The ratio between the powder and isopropanol was maintained at 1:2 by weight throughout the entire process. Additional isopropanol was added as needed to compensate for losses due to evaporation.

Subsequently, the dispersion was filtered, and the resulting material was dried at room temperature for 24 h, followed by an additional drying period at 353 K for 24 h. The dried powder was then heated in an alumina crucible for 48 h at 1473 K in air, using a *RHF1400, Carbolite* muffle furnace. The heating and cooling rate was maintained at 5 K/min. Following the thermal treatment, the final product was manually ground using an agate mortar to achieve the desired powder consistency. If necessary, further processing was conducted using a planetary ball mill.

The phase purity of the samples was analyzed by XRD before the powder was further processed. Similar to earlier studies Klaas et al. [2,28] the samples showed phase purity with minor side phases (see Supporting Information). A representative image of the homogeneous element distribution by EDS can be found in the Supporting Information.

3.2. Production methods of macrostructures

The term 'macrostructure' refers to the classification of the material as granules, foams, or pellets. Macrostructures can offer distinct advantages in practical applications, especially due to their ease of handling compared to powders. In addition, they prevent the formation of preferential flow tunnels through which gases can flow with reduced interaction with the material. It is worth noting that all macrostructures, including granules, foams and pellets, were made from the same powder prepared by the solid-state method to ensure uniform Sr content throughout.

3.2.1. Production method of granules

A wet granulation method Shanmugam [36] was used for the production of granules. A representative image of the resulting granules (**G**) is displayed in Fig. 1. This method has been successfully used in previous work Bulfin et al. [4].

For the preparation of granules, 77 wt% perovskite powder was mixed with 23 wt% microcrystalline cellulose (*Serva,* $d = 0.05$ mm) serving as a binder in an *Eirich EL1* mixing system. These powders were carefully blended to ensure homogeneity. Subsequently, H_2O was added, constituting about 50 wt% of the solid mass, while continuous stirring was maintained until granules were visibly formed.

The resulting granules were dried under atmospheric conditions and sintered in the aforementioned *Carbolite* furnace. The heating rate was 1 K/min. To first decompose the organic material and to avoid rapid gas formation, the granules were heated to 553 K, followed by a further increase to 773 K, where they were held for 2 h at both temperatures. Afterward, for sintering the granules, they were heated to 1573 K for 24 h. The cooling rate to room temperature was 2 K/min.

3.2.2. Production method of foams

The polyurethane (PU) foam replica method Scheffler [37] was utilzed to manufacture the foams, as it has previously proven effective for producing $CaMnO_3$ foams Pein et al. [38]. This method requires fine redox powder with a particle size diameter of $d \leq 10\mu$m to create stable slurries that do not sediment under gravitational influence.

Powder Preparation: To obtain the required fine powder, the $Ca_{0.8}Sr_{0.2}MnO_3$ powder, initially synthesized via the solid-state method, was further refined using a planetary ball mill (*Pulverisette 6, FRITSCH GmbH Milling and Sizing*). Zirconia spheres (diameter: 1 mm) were used for grinding over a period of 30 min, reducing the particle size to $d \approx 10\mu$m. Following grinding, water was added to the powder at a ratio of 5:1 (powder to water). A dispersant (*DOLAPIX 64 CE, Zschimmer & Schwarz*) was added at a concentration 0.84 wt% of solid load, and the mixture was blended for 3 h at a rotation speed of 450 rpm.

Foam Variants: The suspension was separated from the mixing balls using a sieve into a beaker. The resulting foams processed in this manner are designated as $\mathbf{Foam}_{BM}$ (Ball Mill). In an alternative approach, homogenization was achieved with a magnetic stirrer, producing foams labeled $\mathbf{Foam}_{MS}$ (Magnetic Stirring). Both methods followed the same subsequent processing steps. Fig. 2 displays a representative image of $\mathbf{Foam}_{BM}$ and $\mathbf{Foam}_{MS}$.

Please note that, to analyze the particle size distribution of the slurry powders post-mixing, samples were taken during the production process. These samples are designated as $\mathbf{P}_{Foam,BM}$ (for Ball Mill) and $\mathbf{P}_{Foam,MS}$ (for Magnetic Stirring).

Binding and Drying Process: A solid binder (*Optapix PA 4 G, Zschimmer& Schwarz*) was added to the slurry. The mixture was then heated to 353 K for 2 h while stirring continuously, followed by cooling and additional stirring at room temperature for 1 h. The PU foams (*Filterschaum, HSE-FoamTec GmbH*) were then immersed in the slurry, and any excess slurry was removed using a two-plate squeezing machine. The coated foams were air-dried for 24 h.

Fig. 1. Representative image of a granule of $Ca_{0.8}Sr_{0.2}MnO_3$ ($\mathbf{G}_{CS20MO}$) with a diameter of 1.25 mm to 1.6 mm.

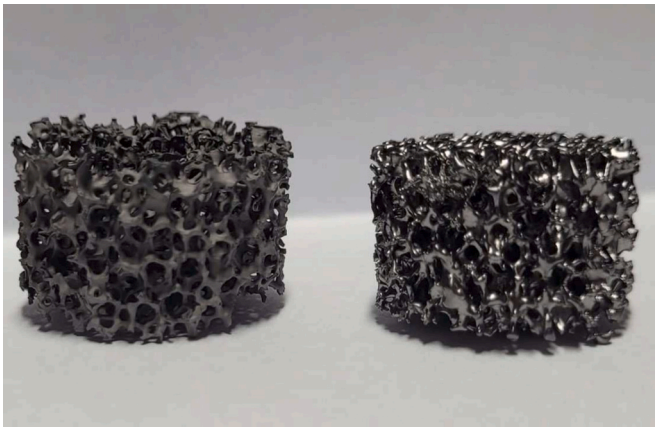

Fig. 2. Image of 20ppi $Ca_{0.8}Sr_{0.2}MnO_3$ foams: $\mathbf{Foam}_{MS}$ (left) and $\mathbf{Foam}_{BM}$ (right).

Debinding and Sintering: The air-dried foams were then transferred to a muffle furnace (*L40/11-BO, Nabertherm*) for debinding and pre-sintering process, adhering to a controlled heating and cooling rate 2 K/min. The procedure began with heating the foams to 353 K for 2 h to eliminate any residual humidity. The temperature was then increased to 553 K for 1 h, followed by 773 K for another 1 h, and finally elevated to 1623 K for 2 h. After cooling to room temperature, the foams were transferred to the *Carbolite* muffle furnace for final sintering at 1623 K for 2 h with heating and cooling rates set at 5 K/min.

Foam Characteristics: This manufacturing process yielded a variety of foams with pore densities ranging from 20 ppi to 60 ppi, as shown in Fig. 3. All samples have a consistent diameter of 20.7 mm and a height of $h \approx 14$ mm. The mass for the samples differed, with 20 ppi weighing 4.46 g, the 30 ppi weighing 5.25 g and the 60 ppi weighing 8.01 g.

3.2.3. Production method of pellets

The pellets were carefully produced using a *Perkin-Elmer* hydraulic press. Initially, 1.25 g of perovskite ($Ca_{0.8}Sr_{0.2}MnO_3$) powder, prepared via the solid-state method, was precisely measured. To consolidate the powder and form the green bodies, a total load of 4×10^4 N was applied to the pressing die. The resulting green bodies were then sintered in a *Carbolite* furnace at 1623 K, maintaining this temperature for 2 h. The heating and cooling rates were set at 5 K/min. The produced pellets exhibited a uniform diameter of 15 mm. A representative image of a pellet can be found in Fig. 4.

The powder used for these pellets can be categorized into two types:

- **Coarser Powder**: This powder was manually ground ($\mathbf{P}_M$). Pellets produced from $\mathbf{P}_M$ are designated as $\mathbf{Pellets}_M$.

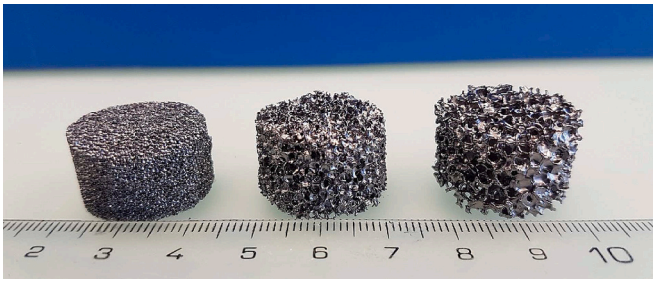

Fig. 3. $Ca_{0.8}Sr_{0.2}MnO_3$ Foams ($\mathbf{Foam}_{BM}$) with different pore densities: 60 ppi (left), 30 ppi (middle) and 20 ppi (right).

Fig. 4. Representative image of a pellet of $Ca_{0.8}Sr_{0.2}MnO_3$.

- **Finer Powder**: This powder was ground using a planetary ball mill ($\mathbf{P}_{BM}$) with zirconia spheres for 30 min at a rotational speed of 450 rpm, employing a ball-to-powder ratio of 2:1. Pellets manufactured from this finer powder are labeled as $\mathbf{Pellet}_{BM}$.

3.3. Crystal structure analysis

The crystallographic structure of the samples was analyzed via powder X-ray diffraction (XRD). The XRD analysis was carried out with a *Bruker D8-Advance (A25)* instrument equipped with a cobalt anode. A *Bruker Lynxeye XE-T* detector was employed for data collection. The samples were prepared on a Si single crystal powder specimen holder. The scanned range was 20° to 130°, with a step size of 0.017°.

The crystallite size D of the different samples was determined by applying the Scherrer formula [39,40] based on the X-ray line width:

$$D = \frac{S\lambda}{\mathrm{FWHM}} cos(\theta)[\mathrm{nm}], \tag{4}$$

where $S = 0.89$ represents the shape factor Pawar and Puri [41], λ is the wavelength of the X-ray, FWHM is the full width at half maximum of the primary peak, and θ is the Bragg's angle of the primary peak.

3.4. Microstructure analysis methods

The term 'microstructure' encompasses structures above the crystal structure level. To explore the microstructure of materials, a diverse range of experimental techniques is employed. These methods are instrumental in providing a comprehensive understanding of the material's microstructure. It is important to note that these microstructural characteristics can exert significant influence on both the kinetic and mechanical properties of the material.

3.4.1. Particle size distribution

The particle size distribution (PSD) was analyzed using a laser scattering particle size distribution analyzer (*Horiba Scientific Partica LA-960, Retsch Technology GmbH*). To achieve this, the powder was dispersed in water and introduced into the measuring chamber. The light source used was a 650 nm laser diode with an output of approximately 5 mW. The detector was a silicon photodiode. The refractive index used for this analysis is 1.67, which was based on the refractive index of $CaMnO_3$ Zhao et al. [42]. From the results of *Pawar* et al. Pawar and Puri [41], it is anticipated that, at the frequencies used, the refractive index is independent of the Sr content.

3.4.2. Scanning electron microscopy

Microstructural analysis of the powders as well as the granules with different Sr contents (as shown in Fig. 5 and Fig. 6) was performed using scanning electron microscopy (SEM). The anaylsis was carried out using a *ZEISS ULTRA 55 FEG* instrument.

The different macrostructures, e.g. pellets and foams, (as illustrated in Fig. 10) were analyzed using a *Hitachi SU3900* instrument featuring a tungsten cathode.

3.4.3. Porosimetry

The porosity and the pore size distribution were measured by mercury porosimetry, using a *Porotec Pascal 140–440* Hg porosimeter from *ThermoFisher Scientific*, with an accuracy of 0.25 %. The specific surface area and the meso- / micropore size distribution were measured via nitrogen porosimetry using a *Porotec Surfer* nitrogen porosimeter from *ThermoFisher Scientific*, with an accuracy of 0.15 %.

3.5. Kinetic analysis methods

The kinetics were analyzed by the thermogravimetric analysis using a *Netzsch STA 409 CD* thermobalance for the investigation of the impact of different pore densities of foams, and by a *STA 449 F3 Jupiter Netzsch* thermobalance for the investigation of the effect of different microstructures. The samples were placed on a flat ceramic sample holder. The gas flow is vertical.

The oxygen partial pressure needed adjustment. Therefore, O_2, Ar and synthetic air (80:20 N_2:O_2 mol %) were mixed. As well, a constant flow through the balance chamber was applied to limit buoyancy effects. For the *Netzsch STA 409 CD* thermobalance, the outlet of this protective gas did not flow through the furnace and thus did not affect the oxygen concentration at the sample.

The samples were reduced at 1173 K under a constant flow of 1 % O_2 in Ar and a total volume flow of 200 ml/min. Afterward, the sample was cooled to the oxidation temperature with a constant flow of 50 ml/min Ar to prevent re-oxidation during the cooling. The heating and cooling rate was 20 K/min. The oxidation temperatures were used in the range of 473 K to 673 K. This temperature window is chosen as in this range; the oxidation is neither too slow so that an oxidation-re-oxidation cycle would take too long nor too fast so that transport limitations due to the mass flow of the reaction gas became relevant.

After cooling the sample to the desired oxidation temperature, 100 ml/min of oxygen (O_2) was introduced to facilitate the oxidation process and oxidize the sample. Following a complete redox cycle as described here, the sample was heated to 873 K under 20 % O_2 in N_2. This step was executed at the beginning of the measurement as well. It serves as a reference state for linear drift correction. Additionally, a blank measurement was conducted to eliminate all parasitic mass changes. For further analysis, only the oxidation segments were used. This process is identical with the process from *Klaas* et al. Klaas et al. [28].

The conversion extent is calculated by

$$X(T) = \frac{\delta_0 - \delta(t)}{\delta_0 - \delta_\infty} \tag{5}$$

$$\delta_0 : \mathrm{non-stoichiometry\ at}\ t = 0$$
$$\delta_\infty : \mathrm{equilibrium\ non-stoichiometry\ the\ sample\ converges\ to.}$$

Earlier studies showed that the samples are completely oxidized for the temperatures analyzed Klaas et al. [28]. Therefore, the equilibrium non-stoichiometry equals zero. To extract the activation energy based on the presented method (Section 2.1), the derivative of the conversion extent needs to be taken. Taking the numerical derivative is problematic since noise is apparent in the raw data. If the complete data set were used for some measurements, the fully-oxidized part would be over-represented. For that reason, a subset of the experimental values is extracted with a discrete step size of 0.05 over the entire range of $X(t)$. This subset is exemplified in Supporting Information. For this subset, the numerical derivative is computed using accurate second-order central differences in the interior points and accurate first-order one-side differences at the edges. This method has been used in previous work. Bulfin et al. [32]; Klaas et al. [28] The following steps are described in

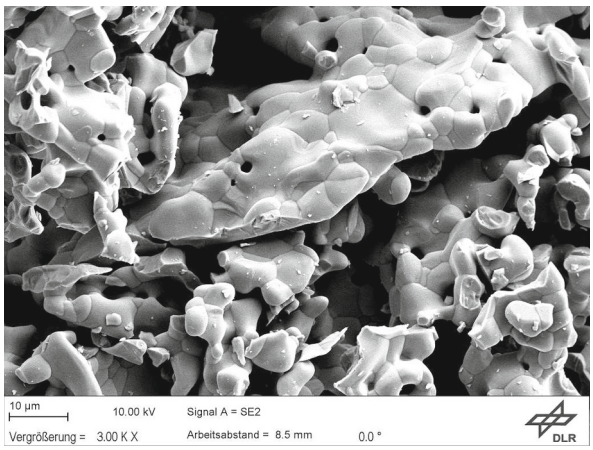

(a) $\mathbf{P}_{\mathrm{CMO}}$

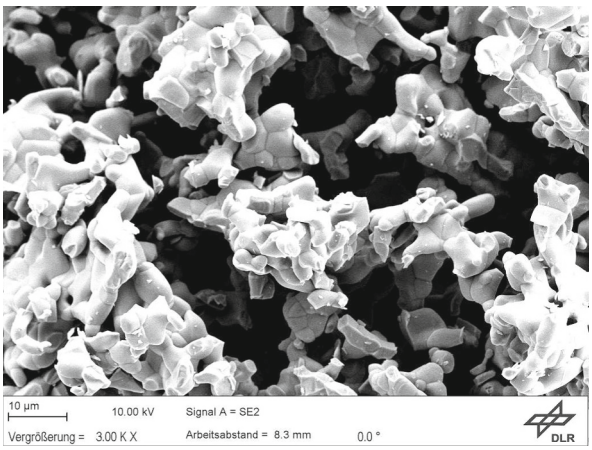

(b) $\mathbf{P}_{\mathrm{CS10MO}}$

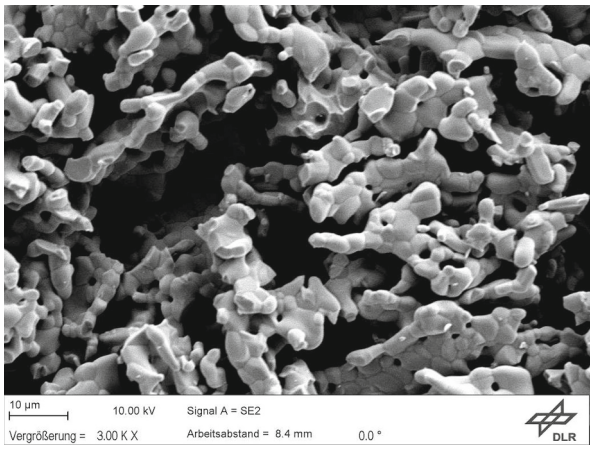

(c) $\mathbf{P}_{\mathrm{CS20MO}}$

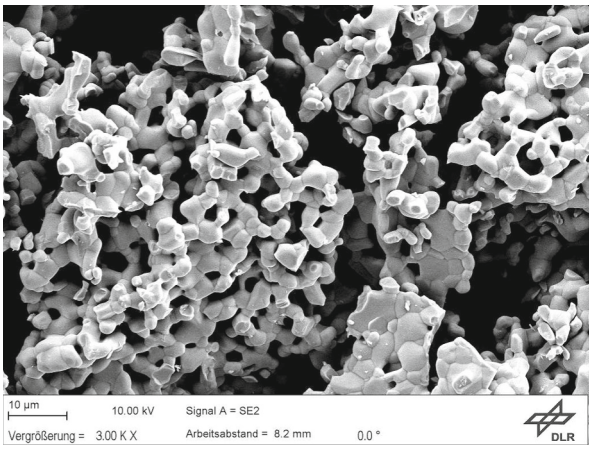

(d) $\mathbf{P}_{\mathrm{CS30MO}}$

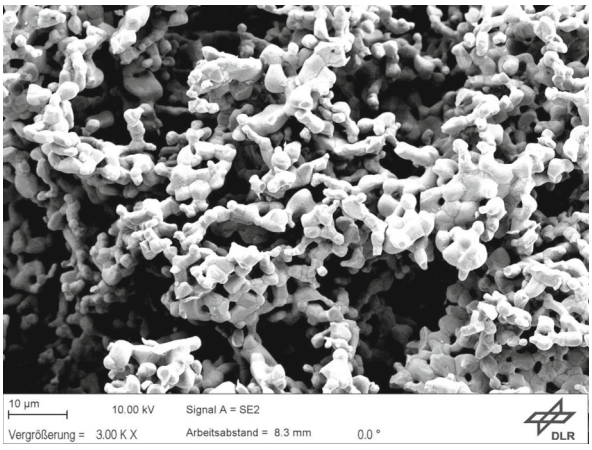

(e) $\mathbf{P}_{\mathrm{CS40MO}}$

Fig. 5. SEM image of powder with varying Sr content. All powders exhibit the agglomeration of small particles; however, particle size varies with Sr concentration. Increasing the Sr content reduces particle size and leads to a more homogeneous particle size distribution compared to samples with lower Sr content.

more detail in Supporting Information.

4. Microstructure analysis

Understanding the microstructure is crucial when working with redox materials, as it significantly impact key properties such as mechanical stability and redox kinetics. Therefore, this section focuses first on the impact of the Sr content on the microstructure of both powder and granules, and then examines how different macrostrucures and their production procedures affect the microscopic structure.

4.1. Material composition dependent microstructure

Fig. 5 displays the SEM image (details in Section 3.4.2) of powder of $Ca_{1-x}Sr_xMnO_3$ with varying Sr concentrations. Starting with Fig. 5a, which displays $CaMnO_3$ without any Sr substitution. The surface

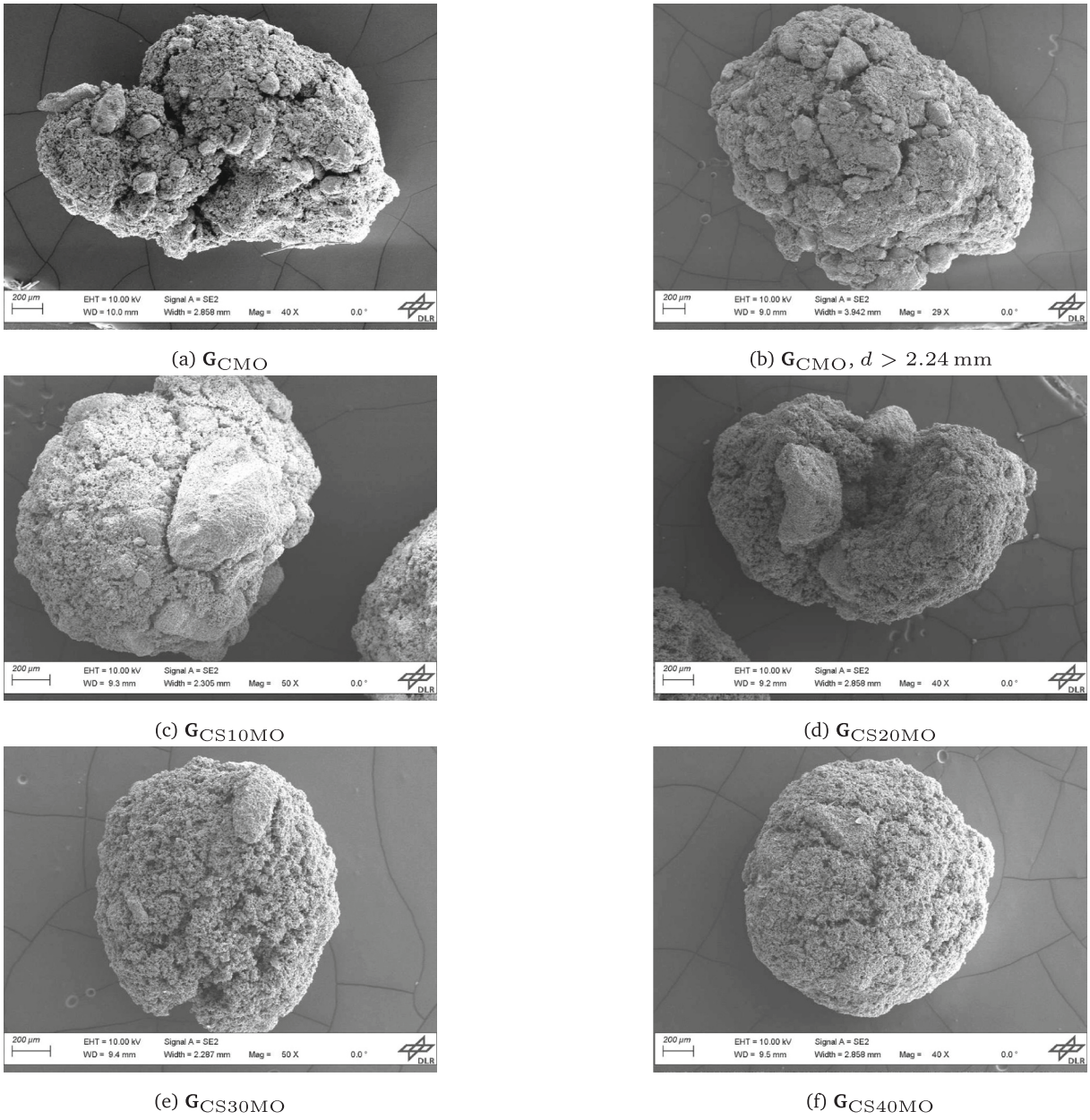

(a) $\mathbf{G}_{\mathrm{CMO}}$ (b) $\mathbf{G}_{\mathrm{CMO}}$, $d > 2.24\,\mathrm{mm}$

(c) $\mathbf{G}_{\mathrm{CS10MO}}$ (d) $\mathbf{G}_{\mathrm{CS20MO}}$

(e) $\mathbf{G}_{\mathrm{CS30MO}}$ (f) $\mathbf{G}_{\mathrm{CS40MO}}$

Fig. 6. SEM image of granules with varying Sr content. All granules exhibit a rough surface, but the homogeneity of the surface depends on the content of Sr.

morphology reveals an agglomeration of small particles. The size of the small particles is spread over a range of $d \approx 3\mu$m to 70μm. Remarkably, the larger particles feature voids with a diameter of $d \approx 1\mu$m and grain boundaries. The size of the grain is between $d \approx 3\mu$m and $d \approx 10\mu$m.

Analyzing the evolution of the microstructure with increasing Sr content, the surface remains an agglomeration of particles. However, it is important to note that the size distribution of the particles changes, as seen in Fig. 5. For example, considering Fig. 5e, which shows the composition with the highest Sr content of 40 %. The powder consists solely of agglomerates of smaller, strongly branched particles. Their size is comparable to the smaller particles mentioned above ($d \approx 3\mu$m). The larger particles with voids and grain boundaries are no longer identifiable, resulting in a homogeneous primary size distribution.

Generally, a substituent may be partially soluble in the principal component, but finally, the solubility limit is reached above which segregation occurs at grain boundaries. The mobility of the ions at the grain boundaries is slowed down by segregated substituent. Leriche et al. [43] Here, Sr is the substituent, and $CaMnO_3$ is the principal component. The decreased mobility leads to smaller crystallites and more grain boundaries for an increasing Sr content.

In addition, the defects in the crystal lattice caused by the substitution can serve as nucleation sites, increasing the number of crystallites and resulting in smaller particles with increasing Sr content. Moreover, several in-situ experiments, such as XRD and SEM, as described by *Li* et al. Li and Deepak [44], would be beneficial to investigate the underlying growth mechanisms further.

The crystallite size of the sample is analyzed by XRD and applying the Scherer equation (details in Section 3.3). The results for 0 %, 20 % and 40 % Sr contents are shown in Table 1. These sample were analyzed to identify trends in crystallite size corresponding to different Sr concentrations. Similar to *Pawar* et al. Pawar and Puri [41], an increase in Sr content correlates with a decrease in crystallite size. This trend supports the previously mentioned hypothesis that defects within the crystal structure are increased.

After analyzing the impact of the Sr content on powder, granules with different Sr contents are examined as well (see Fig. 6). The granules

Table 1
Crystallite size D of different Sr contents calculated by the Scherrer Eq. 4. Besides, the full width at half maximum FWHM and Bragg's angle θ of the major peak are displayed.

Sample	FWHM [°]	θ [°]	D [nm]
$\mathbf{P}_{CMO}$	0.085(8)	39.874(7)	232(22)
$\mathbf{P}_{CS20MO}$	0.088(5)	39.531(2)	170(9)
$\mathbf{P}_{CS40MO}$	0.099(7)	39.401(7)	140(10)

have a diameter of $d = 1.25$ mm to 1.6 mm, except of the granule displayed in Fig. 6b which has a diameter of $d > 2.24$mm. All samples are porous. Similar to the powders, agglomeration of small particles is observed.

This is shown exemplarily in Fig. 7. It displays a close-up of the granule in Fig. 6b. As well, the inhomogeneities in porosity become apparent. Some areas are sintered more densely than others. It is noted that the magnification is smaller in this figure compared to the image of the powders.

The granule with 0 % Sr, shown in Fig. 6a, has an inhomogeneous surface with big trenches which have a width of approximately 95μm. Besides the trenches, denser areas are apparent. This appearance is independent of the total size of the granule (Fig. 6b). The granule with 40 % Sr still features trenches, but they are narrower and less apparent. Moreover, no dense areas are observed. All in all, the surface appears to be more homogeneous.

Analyzing the evolution of the granules with increasing Sr content, a gradual increase in homogeneity of the surface is evident. The implication is that the powder substantially affects the homogeneity of the granules. Leriche et al. [43] The broader distribution of the size of the particles for 0 % Sr results in a more inhomogeneous surface. As the homogeneity of the particles increases, the resulting granule becomes more homogeneous.

The homogeneity of the granules can significantly influence their mechanical stability. For example, trenches have been observed in the granules with 0 %, as described previously. Under mechanical or thermal stress, these features may lead to the easier breakage of the material at these points. Conversely, more densely sintered areas are likely to exhibit greater stability under mechanical load, potentially resulting in larger fragments when fracture occur. In contrast, the more homogeneous sample, e.g., $Ca_{0.6}Sr_{0.4}MnO_3$, may be more resilient to mechanical stress, producing more uniform fragments in the event of a fracture.

To investigate whether the different Sr concentrations of the granules affect their specific surface areas, N_2 porosimetry was conducted

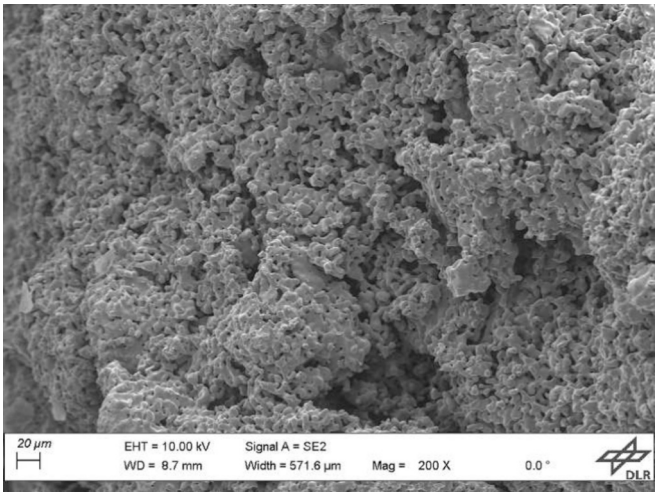

Fig. 7. Close-up of the granule displayed in Fig. 6b. The surface appears to be an agglomeration of small particles. Whereby some surfaces are sintered more densely and others less densely.

(details in Section 3.4.3). The results are displayed in Table 2. It is important to note that these results are close to the detection limit for total surface area measurement, which is approximately 1 m^2, since only a few grams (2 g to 4 g) of sample can be used due to the limitation of the sample holder.

The total size of the granules does not influence the surface area (see Supporting Information). Due to a lack of sufficient samples of $Ca_{0.6}Sr_{0.4}MnO_3$ with diameters between 1.25 mm to 1.6 mm, granules with diameters greater than $d > 2.24$ mm were utilized for the measurement. Generally, the Sr content does not appear to impact the surface area; however, $Ca_{0.6}Sr_{0.4}MnO_3$ showed a slightly higher surface area. This variation may be attributed to inaccuracies arising from the small total surface area being measured. None of the samples displayed meso- or micropores.

The results of mercury porosimetry (details in Section 3.4.3) for the impact of different amounts of Sr are summarized in Fig. 8. The left y-axis displays the normalized cumulative pore volume per g of material, which measures the porosity. Moreover, the total macro-porosity is shown above each curve. The right y-axis displays the differential pore volume distribution. For clarity, the curves are plotted with an offset.

The porosity of the samples shows some variation, with values ranging from 52.74 % ($\mathbf{G}_{CS30MO}$) to 61.05 % ($\mathbf{G}_{CS10MO}$), but no clear trend is observed concerning Sr content. The pore diameters (d_{50}, shown in Table 2) fluctuate n a non-monotonic manner between 8224 nm and 11,447 nm, and the specific surface area values also vary, with $\mathbf{G}_{CS40MO}$ having the highest surface area (0.513 m^2/g) and $\mathbf{G}_{CS20MO}$ the lowest (0.292 m^2/g). These results indicate that Sr content does not systematically affect porosity, pore size distribution, or surface area. Given that all specimens were produced using the same method under identical sintering conditions, the observed variations likely stem from inherent process variability rather than the influence of Sr content. Nevertheless, the general consistency in results suggests that the manufacturing process remains largely reproducible.

Overall, an increasing Sr concentration leads to a more homogeneous agglomeration of the small particles in the powder, which is supported by the development of the crystallite size. This results in a more homogeneous granule with increasing Sr concentration. However, the total surface area and the porosity are not affected by the change in granule appearance.

4.2. Macrostructure and production dependent microstructure

For various applications, not only granules are of interest, but also foam structures Pein et al. [38]. Therefore, this section examines the microstructure of foams produced via two distinct processing routes (Section 3.2.2). Specifically and as mentioned above, the foam prepared with a ball-milled slurry is designated as $\mathbf{Foam}_{BM}$, awhile the foam made using a slurry homogenized by magnetic stirring is referred to as $\mathbf{Foam}_{MS}$. To focus on the impact of the macrostructure alone, $Ca_{0.8}Sr_{0.2}MnO_{3-\delta}$ was used for all samples, chosen for its intermediate Sr concentration among the samples investigated.

The particle size distribution, summarized in Table 3, was analyzed for two differently treated $Ca_{0.8}Sr_{0.2}MnO_3$ powders, as well as for two foam slurries produced through distinct methods. These samples are

Table 2
Summary of pore diameter (d50) and specific surface area measurements of granules **G** with varying Sr content, determined by mercury and nitrogen porosimetry (details in Section 3.4.3). The d50 values show comparable results across different Sr levels without a discernible trend.

Sample	d50 [nm]	surface area [m^2/g]
$\mathbf{G}_{CMO}$	10,475	0.311
$\mathbf{G}_{CS10MO}$	11,259	–
$\mathbf{G}_{CS20MO}$	8224	0.292
$\mathbf{G}_{CS30MO}$	11,447	–
$\mathbf{G}_{CS40MO}$	9292	0.513

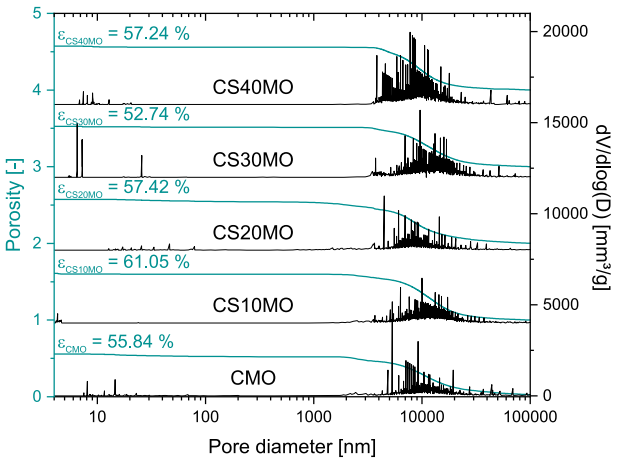

Fig. 8. Sr content dependent porosity determined by Hg porosimetry (exp. details in Section 3.4.3). Displayed are the normalized cumulative pore volume per g of material which is a measure for the porosity (left axis) and the differential pore volume distribution (right axis). Additionally, the total porosity **ò** is assigned for each sample.

Table 3
Particle size distribution of used powders of $Ca_{0.8}Sr_{0.2}MnO_3$ measured via a laser scattering particle size distribution analyzer (details in Section 3.4.1).

Sample	d50 [μm]	Mean [μm]	Standard Dev. [μm]
$\mathbf{P}_{M}$	16.7	108.8	139.2
$\mathbf{P}_{BM}$	6.6	6.9	2.2
$\mathbf{P}_{Foam,BM}$	3.1	3.4	1.5
$\mathbf{P}_{Foam,MS}$	5.0	5.3	2.2

designated as $\mathbf{P}_{M}$, $\mathbf{P}_{BM}$, $\mathbf{P}_{Foam,MS}$ and $\mathbf{P}_{Foam,BM}$ (details in Section 3.2.2).

The PSD shows that, as expected, the manually ground powder $\mathbf{P}_{M}$ has the largest mean particle size (d50), and the broadest distribution width. Ball-milling ($\mathbf{P}_{BM}$) effectively decreases both the mean particle size and the PSD, resulting in narrower distribution of particle size. Further ball-milling of the suspension reduces the PSD width even more, with the mean particle size halving compared to $\mathbf{P}_{BM}$. In contrast, additional magnetic stirring primarily breaks down powder agglomerates, resulting in only a slight decrease in mean particle size with minimal effect on PSD width. The standard deviation (SD) in each PSD supports these observations, indicating reduced variability with each successive milling step, while magnetic stirring alone produces only minor changes in particle size distribution.

Fig. 9 shows the $Ca_{0.8}Sr_{0.2}MnO_3$ foams produced by the two procedures outlined. Both structures display similar characteristics, with triangular-shaped struts, which are hollow - a feature previously observed in similar materials manufactured using this process Pein et al. [38]. This hollow, triangular strut structure is typical of ceramic foams produced by the polyurethane replica method and results from the sublimation of the PU foam template used. Studart et al. [45]; Betke et al. [46] Some surface defects, such as cracks and voids, are noticeable.

A distinction between the two samples can already be observed: $\mathbf{Foam}_{MS}$, made from $\mathbf{P}_{Foam,MS}$, has a rougher surface, whereas $\mathbf{Foam}_{BM}$, made from $\mathbf{P}_{Foam,BM}$, appears smoother. The surface difference between these structures will be analyzed in more detail in the following sections.

After examining the foam shapes, the focus shifts to analyzing the different surface properties of the samples. To compare the effects of shape and treatment, pellets were produced with two distinct powder treatments as detailed in Section 3.2.3. The pellet produced with ball-milled powder ($\mathbf{P}_{BM}$) is labeled $\mathbf{Pellet}_{BM}$, while the pellet with manually milled powder ($\mathbf{P}_{M}$) is labeled $\mathbf{Pellet}_{M}$, as previously outlined.

A close-up SEM image of the surfaces of all samples, all composed of $Ca_{0.8}Sr_{0.2}MnO_3$, is presented in Fig. 10. The surface of $\mathbf{Pellet}_{BM}$ (Fig. 10a) is densely sintered surface, showing grain boundaries and several pores with diameters of $d \approx 1\,\mu$m. In contrast, $\mathbf{Pellet}_{M}$ (Fig. 10b) displays a less dense sintered surface. Overall, the surface appears to be composed of polycrystalline regions interspersed with less dense areas.

The $\mathbf{Foam}_{BM}$ (Fig. 10c) also exhibit densely sintered surface with visible grain boundaries, similar to the $\mathbf{Pellet}_{BM}$. However, unlike the pellet, no voids are apparent in the foam; instead, a trench with a width below 1 μm is visible, which may have formed due to gas evaporation during debinding.

In contrast, the surface of $\mathbf{Foam}_{MS}$ (Fig. 10d) resembles that of $\mathbf{Pellet}_{M}$, featuring a rough texture without densely sintered areas. The grains are smaller than those in $\mathbf{Foam}_{BM}$, with a diameter of $d \approx 5\,\mu$m.

The granule (Fig. 10e) also shows a porous surface, consisting of polycrystalline small particles with a coral-like appearance.

To assess the impact of shape on crystallite size, measurements were conducted for each form (see Table 4). Consistent with the SEM observations, the sample with a densely sintered surface, $\mathbf{Foam}_{BM}$, exhibits the largest crystallite size, while $\mathbf{Foam}_{MS}$ has a smaller crystallite size. Interestingly, the granule and $\mathbf{Foam}_{MS}$ share a similar crystallite size, comparable to that of the powder. The crystallite size of $\mathbf{Foam}_{BM}$,

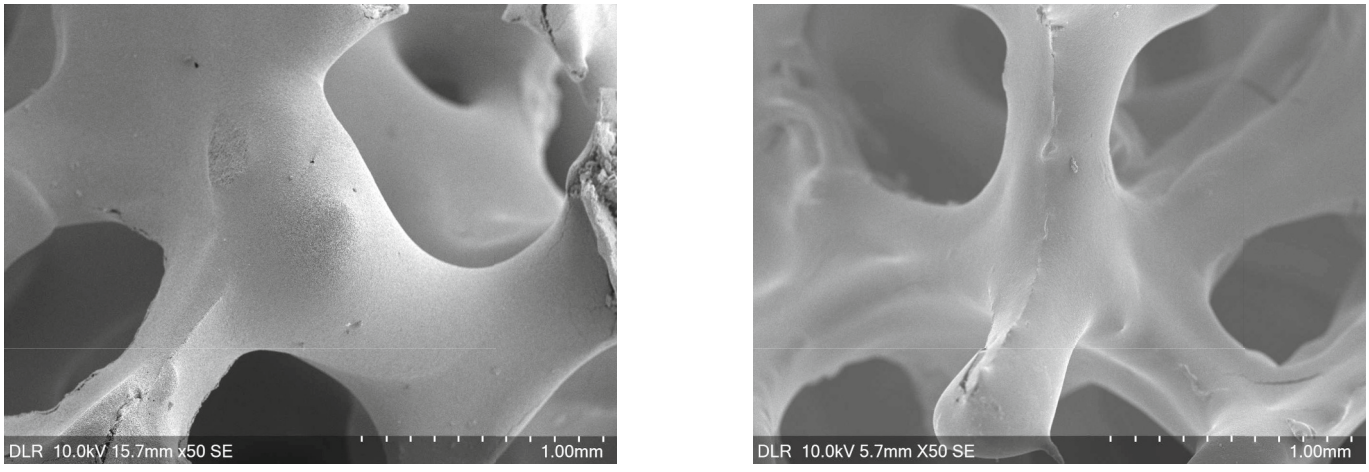

(a) $\mathbf{Foam}_{MS}$ (b) $\mathbf{Foam}_{BM}$

Fig. 9. SEM of the shape of the foams. Both foams exhibit a typical structure with struts having a triangular shape. Already indicated here is a difference in the surface since $\mathbf{Foam}_{MS}$ appears to have a rougher surface, since it is less shiny.

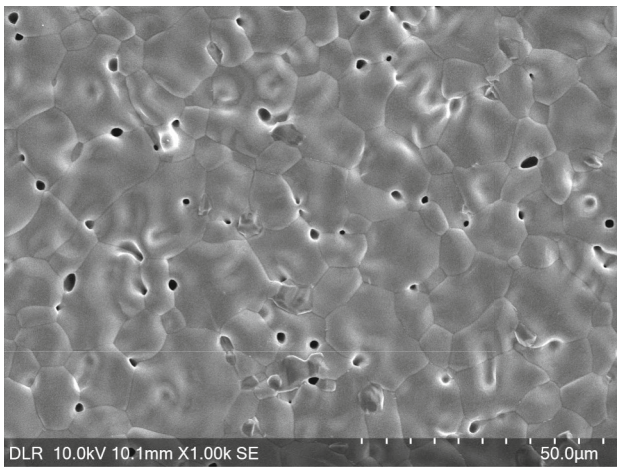

(a) $\text{Pellet}_{\text{BM}}$

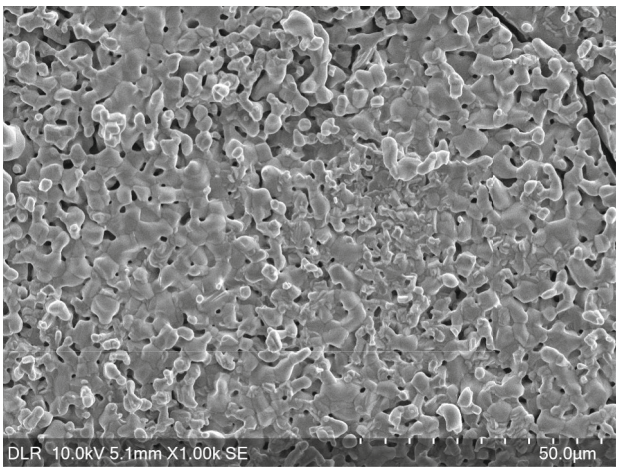

(b) Pellet_{M}

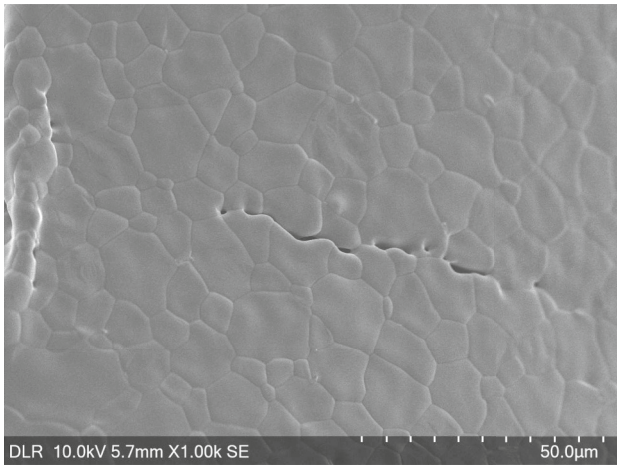

(c) Foam_{BM}

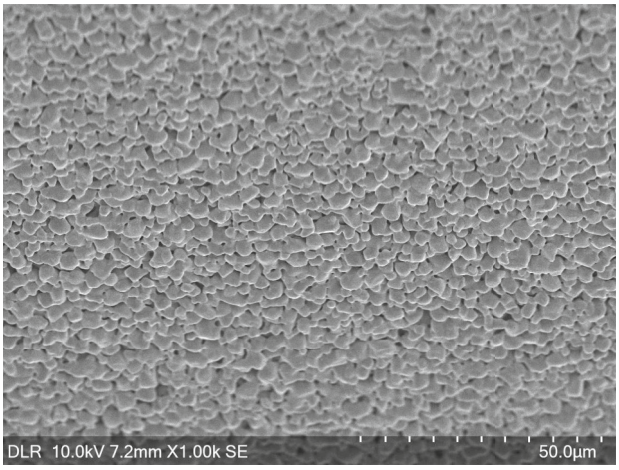

(d) Foam_{MS}

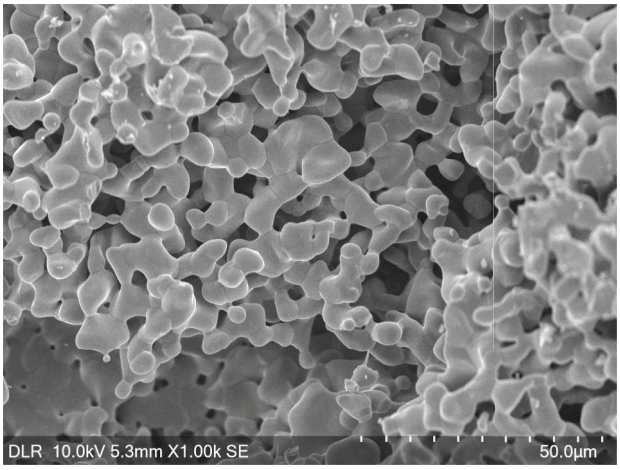

(e) Granule

Fig. 10. SEM close-up of different macrostructures and production procedures. All samples are $Ca_{0.8}Sr_{0.2}MnO_3$. Highlighted is that the underlying powder governs the difference in the surface structure. Finer powder ($\mathbf{P}_{\text{BM}}$, $\mathbf{P}_{\text{Foam,BM}}$) results in a denser sintered surface compared to coarser powder($\mathbf{P}_{\text{MS}}$, $\mathbf{P}_{\text{Foam,MS}}$), which leads to larger specific surface area and higher micro-porosity.

however, is significantly larger than that of the powder.

The surface area for different macrostructures is summarized in Table 5 to further analyze the morphology. $\mathbf{Foam}_{\text{MS}}$ exhibits the highest surface area, which is expected due to its rough surface. $\mathbf{Foam}_{\text{BM}}$ has approximately half the surface area of $\mathbf{Foam}_{\text{MS}}$, while the granules possess a slightly smaller surface area. This difference can be attributed to the hollow struts in the foams; when these struts are cracked open, the internal surfaces contribute additional surface area. Although the exact values should be interpreted cautiously due to their proximity to the detection limit, the observed deviation is significant enough to suggest

Table 4
Crystallite size D of different macrostructures and production procedures, calculated by the Scherrer eq. 4. Besides, the full width at half maximum FWHM and Bragg's angle θ of the major peak are displayed. All samples are $Ca_{0.8}Sr_{0.2}MnO_3$.

Sample	FWHM [°]	θ [°]	D [nm]
$\mathbf{P_M}$	0.088(5)	39.531(2)	170(9)
G	0.086(3)	39.530(1)	175(7)
$\mathbf{Foam_{BM}}$	0.055(2)	39.472(1)	262(9)
$\mathbf{Foam_{MS}}$	0.092(4)	39.478(3)	158(7)

Table 5
Summary of pore diameter (d50) and specifiv surface area measurements of different macrostructure, determined by mercury and nitrogen porosimetry (details in Section 3.4.3).

Sample	d50 [nm]	surface area [m^2/g]
$\mathbf{G_{CS20MO}}$	8224	0.292
$\mathbf{Foam_{MS}}$	1528	1.117
$\mathbf{Foam_{BM}}$	45,059	0.598
$\mathbf{Pellet_M}$	1689	–
$\mathbf{Pellet_{BM}}$	143	–

that $\mathbf{Foam_{MS}}$ has an increased surface area. Similar to the granules, neither of the foams exhibits micro- or mesopores.

When analyzing the porosity of the different macrostructures and production procedures, it becomes evident that samples produced with a narrower particle size distribution powder exhibit lower porosity compared to their counterparts with wider distribution as shown in Fig. 11. Among the samples, $\mathbf{Pellet_{BM}}$ demonstrates the lowest porosity of 2.77 %, while $\mathbf{Foam_{MS}}$ shows the highest porosity of 57.42 %, a value comparable to that of the granules. These porosity trends align with the surface analysis conducted via SEM.

The d50 value of the pore size distribution is displayed in Table 5. Notably, $\mathbf{Foam_{BM}}$ exhibits the highest d50 value (d50 = 45,059 nm), indicating that majority of measured pores fill the hollow struts. In contrast, $\mathbf{Foam_{MS}}$ and $\mathbf{Pellet_M}$ have similar d50 values, while the granules show a slightly higher d50, likely due to the substantial binder content (23 wt%) used during production. $\mathbf{Pellet_{BM}}$ display the smallest d50, reinforcing the SEM results.

It is important to highlight that the particle size distribution of the powder used in the production of the different macrostructures plays a critical role in determining the microstructure of the resulting samples. Finer powder results in a denser sintered surface, whereas coarser powders yield more porous structures with a rough surface, even under otherwise identical conditions. This observation aligns with previous research that has demonstrated the positive impact of finer powder on sintering behavior, particularly in the production of ceramic pellets. Ferkel and Hellmig [47] Furthermore, the differences between various macrostructures, such as pellets and foams, can be explained by two factors. First, the addition of organic material, which decomposes during subsequent processing, results in less dense material as the organics evaporate, creating voids due to the lack of material. Additionally, gases can form tunnels within the material during this process. Second, the application of pressure during pellet production compresses the material, leading to higher density, which is favorable for sintering Riedel and Chen [48].

All in all, the results show that a smaller particle size distribution of the perovskite powder used leads to a denser sintered sample. This is reflected in larger crystallite sizes, a smaller surface area and lower porosity.

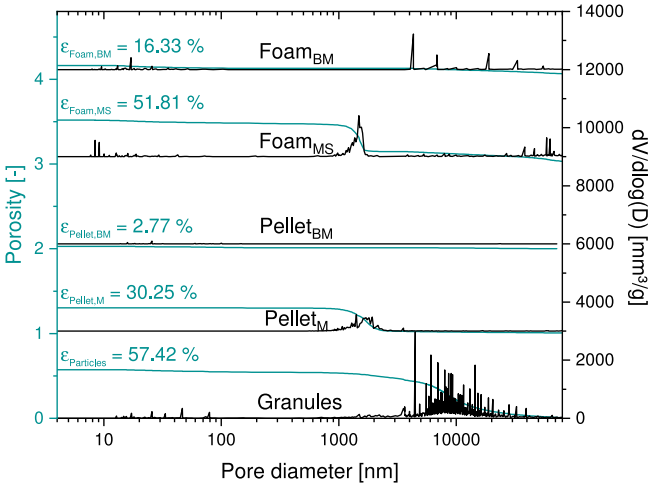

Fig. 11. Macrostructure dependent porosity for $Ca_{0.8}Sr_{0.2}MnO_3$. Displayed are the normalized cumulative pore volume per g of material, which measures the porosity (left axis) and the differential pore volume distribution (right axis). Additionally, the total porosity **ò** is assigned for each sample.

5. Microstructure dependent kinetics

As presented in the first part of the study, the microstructure is affected by both the material composition as well as the processing of the powder. The following part of the study investigates the impact of these microstructural changes on the oxidation kinetics.

5.1. Impact of the varying Sr concentration

The impact of the Sr content on the oxidation kinetics was previously analyzed before. Imponenti et al. [49]; Klaas et al. [28] *Klaas* et al. Klaas et al. [28] demonstrate that an increase in the Sr content leads to faster oxidation kinetics. This acceleration is mainly attributed to the decrease in activation energy with an increasing Sr content, primarily due to changes in crystal structure. Higher Sr content results, on the one hand, in reduced orthorhombic distortion and, on the other hand, to a longer A-O2 bond length. Klaas et al. [2]

The impact of microstructure on the kinetics was neglected in the study by *Klaas* et al. However, the study indicates that Sr concentration influences the material's morphology. As shown in Table 2, Sr concentration does not affect micro-porosity or pore diameter, indicating no significant change in the microstructure. In contrast, SEM images (Fig. 6) clearly demonstrate that Sr content alters the morphology, affecting surface characteristics. Therefore, while the microstructure remains largely unchanged, the observed morphological differences suggest that Sr-induced surface modifications could still play a role in oxidation kinetics, alongside other influencing factors discussed above.

5.2. Impact of the microstructure of $Ca_{0.8}Sr_{0.2}MnO_3$ (Macrostructures)

In the following, a material composition is selected to investigate exclusively the effect of different microstructures. Therefore, only $Ca_{0.8}Sr_{0.2}MnO_{3-\delta}$ is further analyzed, chosen due to its average Sr content among the studied samples. Since different macrostructures are investigated in addition to different microstructures. The first step is to analyze how the different macrostructures affect the oxidation kinetics.

The previous study indicated that variations in the diameter of a granule (d_{min} = 1.25 mm, d_{max} > 2.24 mm) do not affect the oxidation kinetics. Klaas et al. [28] The evolution of the conversion extent $X(t)$ at T_{ox} = 593 K for granules with different diameters of *Klaas* et al. Klaas et al. [28] are shown in Fig. 12. The initial reduction extents at the beginning of the oxidation step are similar and displayed in the Supporting Information.

Moreover, Fig. 12 displays the oxidation curve of foams ($\mathbf{Foam_{BM}}$) with different pore densities. All foams displayed here are produced by a ball-milled slurry. To identify if the total mass impacts the oxidation

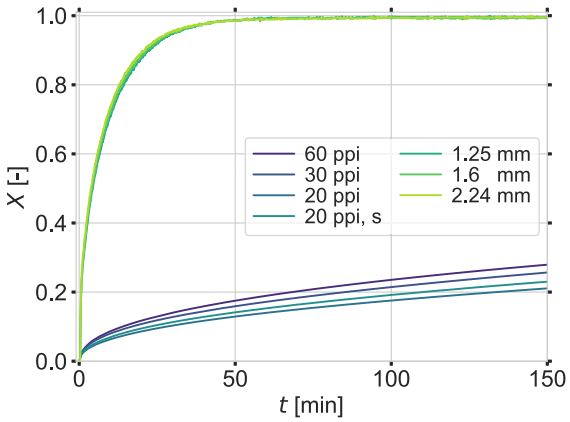

Fig. 12. Evolution of the conversion extent for different sizes of granules (**G**) of $Ca_{0.8}Sr_{0.2}MnO_{3-\delta}$ (from *Klaas* et al. Klaas et al. [28]) and foams (**Foam**$_{BM}$) of $Ca_{0.8}Sr_{0.2}MnO_{3-\delta}$ with different pore densities at $T_{Ox} = 593$ K. The foams were produced with $P_{Foam,BM}$ powder. The displayed diameter is the minimal diameter of the granule. The conversion extent is independent of the granular size within the measured diameter range. Moreover, the different pore densities do not highly affect the oxidation behavior. Contrary, the difference between the granule and the foams is striking.

curve, the sample '20 ppi, s' weighs 57 % of sample '20 ppi', resulting in slightly faster oxidation kinetics due to the reduced mass. All masses of the oxidized samples are displayed in Supporting Information.

The oxidation rate increases slightly with increasing pore density, accompanied by an increase in total sample mass as the size of the pores decreases, making the foam becomes more compact (see Fig. 3). Since a decrease in mass leads to slightly faster oxidation kinetics, the trend towards an increase in oxidation rate with increasing pore density is opposite to the effect of mass. Nevertheless, the different oxidation behavior for the different pore densities can be attributed to changing heat transfer properties. The effect is small compared to the change in pore density. At this point, it should be emphasized that all the results presented in this section are below the mass transfer limit of 2.35 mg/s.

Apart from the minor influences of pore density and mass, the difference between foam and granules is particularly striking. The granules oxidize much faster than the foam. As known from the previous section, these two macrostructures (**G** and **Foam**$_{BM}$)) also differ in their microstructure.

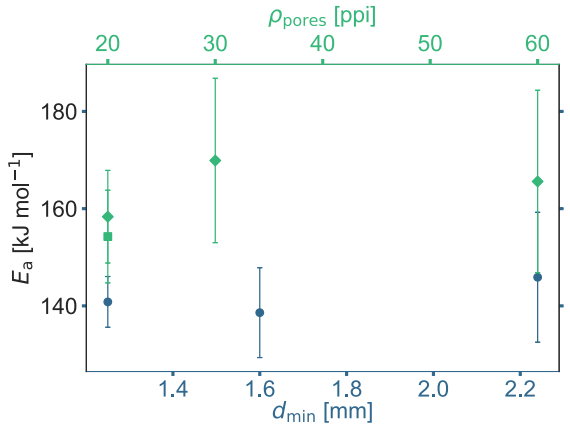

Fig. 13. Activation energy of the oxidation for different granules (**G**) and foams (**Foam**$_{BM}$). The lower blue x-Axis shows the minimal diameter of the granule, and the upper green x-Axis shows the pore density. The square assigns the smaller foam of 20 ppi with 57 % of the weight. (For interpretation of the references to colour in this figure legend, the reader is referred to the web version of this article.)

The activation energy for all samples presented above was extracted by the isoconversional method (details in Section 2.1). Fig. 13 emphasizes that the activation energy of all granules is identical within the experimental uncertainty. The activation energy of all foams is also comparable. Comparing the activation energy of both macrostructures, granules and foam, shows that they overlap within the experimental error. Furthermore, the foams appear to have slightly higher activation energy, but since the mass change from mg for granules to g for foams is enormous, this small change should not be over-interpreted.

To further investigate the impact of the material's structure, foams and pellets with different microstructures are analyzed additionally. The labeling for the foams and pellets is as presented above. The foams have 20 ppi. The results are displayed in Fig. 14. Upon examining the graph, we observe that it exhibits a monotonic behavior, indicating that the response consistently trends in one direction over time. This is an important characteristic, as it reflects the stability of the materials' performance across the different microstructures tested. Each curve represents a different sample, and while the time constants remain consistent among them, the specific response of each sample varies based on its unique structural attributes. It is important to note that this analysis is qualitative in nature and serves to highlight the trends and behaviors of the materials tested. A more detailed quantitative analysis will be conducted in future work to provide deeper insights into the relationships between structure and performance metrics. The initial reduction extents are similar and displayed in Supporting Information. The Supporting Information additionally contains the masses of the oxidized samples.

Focusing first on the different pellets, the increased oxidation kinetics of **Pellet**$_{M}$ compared to **Pellet**$_{BM}$ is striking. The same trend holds comparing **Foam**$_{MS}$ with fast kinetics compared to **Foam**$_{BM}$ with slow kinetics. The samples with slow kinetics are not fully oxidized within 150 min, and **Foam**$_{BM}$ has the slowest oxidation kinetics. The kinetics of the granules is comparable to both, **Foam**$_{MS}$ and **Pellet**$_{M}$. Here, **Foam**$_{MS}$ has the fastest kinetics, followed by **Pellet**$_{M}$ and the granules.

The similar activation energy of granules and foams indicates that the determined activation energy is a material characteristic quantity independent of the specimen's macrostructure.

The striking difference between the samples is their microstructure (see Fig. 10). The previous presented and discussed results are summarized in Table 6. The results showed that a smaller particle size distribution of the powder used for the production of the macrostructures leads to denser sintered samples. This is highlighted by the larger crystallite sizes, the smaller surface area and the lower porosity.

Yang et al. Yang and Lin [50] as well observed microstructure-dependent oxidation kinetics in perovskites, although they used CO_2 as the oxygen source.

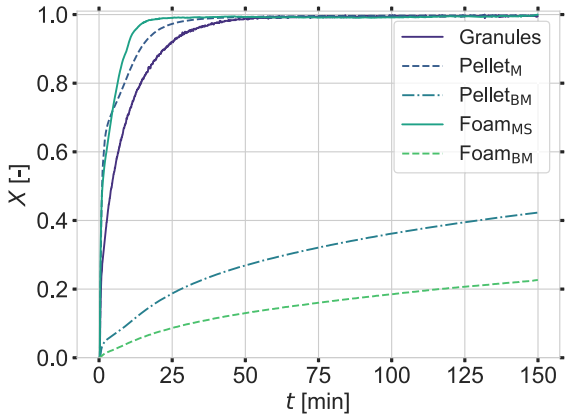

Fig. 14. Oxidation curves for different structures and production procedures at $T_{Ox} = 593$ K. The granule has a diameter of 1.25 mm. Microstructural changes govern the changing oxidation kinetics.

Table 6
Summary of the relevant information of Section 4 to analyze the impact of the microstructure on the oxidation kinetics as presented in Fig. 14. All samples consists of $Ca_{0.8}Sr_{0.2}MnO_3$. The granules have a diameter of 1.25 mm to 1.6 mm.

Sample	Surface area [m^2/g]	Crystallite size [nm]	Porosity [%]
G	0.292	175	57.42
Pellet$_M$			30.25
Pellet$_{BM}$			2.77
Foam$_{MS}$	1.117	158	51.81
Foam$_{BM}$	0.598	262	16.33

A previous study highlighted the independence of oxidation from $Ca_{0.8}Sr_{0.2}MnO_{3-\delta}$ from the oxygen partial pressure. Klaas et al. [28] Therefore, the oxygen dependence will not be further analyzed here. Moreover, this implies that oxidation is not limited by adsorption but by bulk diffusion.

Kimura et al. Kimura et al. [51]; Kimura [52] described that the oxidation kinetics is inversely proportional to the particle size of the sample. The term 'particle' will be used in the following to describe the size of the individual unit of a macrostructure. E.g. for the granule, the term 'particle' describes the individual small particle. Thus, considering the presented samples as an agglomeration of particles, where the particle size is different for each sample, the oxidation kinetics follows the proposed trend.

To reconsider the different microstructures, the reader is referred to Section 4.2. The sample **Foam$_{BM}$** is densely sintered and thus has the biggest particle size. For this sample, the particle size of the sample is determined by the thickness of the struts. This sample shows the slowest oxidation kinetics. The corresponding **Foam$_{MS}$** has smaller particles and faster oxidation kinetics. The same statement holds for the granules. **Pellet$_M$** consists of mainly smaller particles and some sintered areas with larger particles. This explains the initial faster oxidation kinetics and decelerating after 1 min.

Additionally, diffusion of ions along crystallite boundaries proceeds faster than diffusion of ions through the bulk. Kingery et al. [53]; Kimura [52] The samples which are less dense sintered have more boundaries, leading to faster kinetics.

The depth-dependent diffusion of oxygen may be analyzed to investigate the above hypothesis further. This can be realized by ^{18}O-secondary ion mass spectrometry. For this purpose, a sample is reduced, then partially oxidized with the tracer oxygen ^{18}O, and subsequently, the depth-dependent ^{18}O concentration is measured. In this way, oxygen diffusion can be studied layer by layer for different oxidation times.

6. Conclusion

Building upon the prior work of *Klaas* et al. Klaas et al. [2], the results presented in this study provide valuable insights into the microstructural characteristics of $Ca_{1-x}Sr_xMnO_3$ powder, granules, pellets and foams. The SEM analysis of the powder revealed that as Sr content increases, the size distribution of the particles changes, with higher Sr concentrations leading to smaller, more homogeneous particles. This is attributed to the decrease mobility of ions at grain boundaries due to segregated Sr substituent, which result in smaller crystallites and more grain boundaries. Defects in the crystal caused by Sr substitution also contribute to smaller crystallite size and more numerous crystallites. XRD analysis confirmed the trend of decreasing crystallite size with increasing Sr content, supporting the hypothesis that defects introduced by Sr substitution reduce crystallite size. The nitrogen porosimetry of the different macrostructures and production methods demonstrated that the powder particle size distribution significantly impact the surface area and porosity of the final structure. Samples prepared with finer powder show a denser sintered surface, while samples with coarser powder show a more porous structure. These differences in microstructure play a crucial role in influencing oxidation kinetics: dense sintered surfaces exhibit slower oxidation kinetics, while porous surfaces exhibit faster kinetics, and this relationship inversely correlates with particle size. Furthermore, this study highlights the role of ion diffusion, with diffusion along crystallite boundaries accelerating the kinetics. It is noteworthy that the activation energy remains the same for both macro- and microstructures. In summary, these results provide valuable insights for material design and optimization in specific applications. Further research, in particular studies on depth-dependent oxygen diffusion, promises to provide deeper insights into the mechanisms responsible for the observed trends. Moreover, the effect of other dopants on the microstructure and the oxidation kinetics will provide further understanding and will help to draw more general conclusions about the material.

CRediT authorship contribution statement

Lena Klaas: Writing – review & editing, Writing – original draft, Visualization, Methodology, Investigation, Conceptualization. **Asmaa Eltayeb:** Writing – review & editing, Writing – original draft, Methodology, Investigation, Conceptualization. **Dorottya Kriechbaumer:** Supervision, Resources, Funding acquisition. **Martin Roeb:** Writing – review & editing, Supervision, Resources, Funding acquisition. **Christian Sattler:** Supervision, Resources.

Declaration of competing interest

The authors declare the following financial interests/personal relationships which may be considered as potential competing interests:

This work has received funding from project SesAm (EFRE-0801808), which is co-funded by the state of Northrhine-Westphalia, Germany, and the European EFRE fund and IN2SOLAIR (SURPF2101290008), which is part of the SFERA-III Transnational Access Program. If there are other authors, they declare that they have no known competing financial interests or personal relationships that could have appeared to influence the work reported in this paper.

Acknowledgements

This work has received funding from project SesAm (EFRE-0801808), which is co-funded by the State of Northrhine-Westphalia, Germany, and the European EFRE fund and IN2SOLAIR (SURPF2101290008), which is part of the SFERA-III Transnational Access Program. The authors thank Nils Rahner for performing the PSD measurements and Mathias Pein and Gözde Alkan for performing SEM and EDS.

Appendix A. Supplementary data

Supplementary data to this article can be found online at https://doi.org/10.1016/j.ssi.2025.116803.

Data availability

Data will be made available on request.

References

[1] E.I. Goldyreva, I.A. Leonidov, M.V. Patrakeev, A.V. Chukin, I.I. Leonidov, V. L. Kozhevnikov, J. Alloys Compd. 638 (2015) 44–49.
[2] L. Klaas, M. Pein, P. Mechnich, A. Francke, D. Giasafaki, D. Kriechbaumer, C. Agrafiotis, M. Roeb, C. Sattler, Physical chemistry chemical physics 24 (2022) 27976–27988.
[3] C. Agrafiotis, M. Pein, D. Giasafaki, S. Tescari, M. Roeb, C. Sattler, Journal of Solar Energy Engineering 141 (2019).
[4] B. Bulfin, J. Lapp, S. Richter, D. Gubàn, J. Vieten, S. Brendelberger, M. Roeb, C. Sattler, Chem. Eng. Sci. 203 (2019) 68–75.

[5] M. Pein, C. Agrafiotis, J. Vieten, D. Giasafaki, S. Brendelberger, M. Roeb, C. Sattler, Solar Energy 198 (2020) 612–622.
[6] Z. Yang, Y.S. Lin, Y. Zeng, Industrial & Engineering Chemistry Research 41 (2002) 2775–2784.
[7] J. Vieten, B. Bulfin, F. Call, M. Lange, M. Schmücker, A. Francke, M. Roeb, C. Sattler, J. Mater. Chem. A 4 (2016) 13652–13659.
[8] H.E. Bush, N.P. Nguyen, T. Farr, P.G. Loutzenhiser, A. Ambrosini, Solid State Ion. 368 (2021) 115692.
[9] J. Vieten, B. Bulfin, D.E. Starr, A. Hariki, F.M.F. de Groot, A. Azarpira, C. Zachäus, M. Hävecker, K. Skorupska, N. Knoblauch, M. Schmücker, M. Roeb, C. Sattler, Energ. Technol. 7 (2019) 131–139.
[10] M. Ezbiri, A. Reinhart, B. Huber, K.M. Allen, A. Steinfeld, B. Bulfin, R. Michalsky, React. Chem. Eng. 5 (2020) 685–695.
[11] T.P. Farr, N.P. Nguyen, E. Bush, A. Ambrosini, P.G. Loutzenhiser, Materials 13 (2020) year.
[12] M. Tang, L. Xu, M. Fan, Appl. Energy 151 (2015) 143–156.
[13] N. Galinsky, A. Mishra, J. Zhang, F. Li, Appl. Energy 157 (2015) 358–367.
[14] G. Luongo, F. Donat, C.R. Müller, Physical chemistry chemical physics 22 (2020) 9272–9282.
[15] A. Riaz, P. Kreider, F. Kremer, H. Tabassum, J.S. Yeoh, W. Lipiński, A. Lowe, ACS Applied Energy Materials 2 (2019) 2494–2505.
[16] A.H. McDaniel, E.C. Miller, D. Arifin, A. Ambrosini, E.N. Coker, R. O'Hayre, W. C. Chueh, J. Tong, Energ. Environ. Sci. 6 (2013) 2424.
[17] A.H. McDaniel, A. Ambrosini, E.N. Coker, J.E. Miller, W.C. Chueh, R. O'Hayre, J. Tong, Energy Procedia 49 (2014) 2009–2018.
[18] A.A. Emery, J.E. Saal, S. Kirklin, V.I. Hegde, C. Wolverton, Chem. Mater. 28 (2016) 5621–5634.
[19] M. Kubicek, A.H. Bork, J.L.M. Rupp, J. Mater. Chem. A 5 (2017) 11983–12000.
[20] X. Qian, J. He, E. Mastronardo, B. Baldassarri, C. Wolverton, S.M. Haile, Chem. Mater. 32 (2020) 9335–9346.
[21] S.M. Babiniec, E.N. Coker, J.E. Miller, A. Ambrosini, Int. J. Energy Res. 40 (2016) 280–284.
[22] L. Imponenti, K.J. Albrecht, J.W. Wands, M.D. Sanders, G.S. Jackson, Sol. Energy 151 (2017) 1–13.
[23] E. Mastronardo, X. Qian, J.M. Coronado, S.M. Haile, J. Mater. Chem. A 8 (2020) 8503–8517.
[24] R. Buck, C. Agrafiotis, S. Tescari, N. Neumann, M. Schmücker, Frontiers in Energy Research 9 (2021).
[25] J. Vieten, B. Bulfin, M. Senholdt, M. Roeb, C. Sattler, M. Schmücker, Solid State Ion. 308 (2017) 149–155.
[26] F. Jin, C. Xu, H. Yu, X. Xia, F. Ye, X. Li, X. Du, Y. Yang, ACS Appl. Mater. Interfaces 13 (2021) 3856–3866.
[27] M.W. Gaultois, T.D. Sparks, C.K.H. Borg, R. Seshadri, W.D. Bonificio, D.R. Clarke, Chem. Mater. 25 (2013) 2911–2920.
[28] L. Klaas, B. Bulfin, D. Kriechbaumer, M. Roeb, C. Sattler, Physical chemistry chemical physics 25 (2023) 9188–9197.
[29] P. Majewski, L. Epple, F. Aldinger, J. Am. Ceram. Soc. 83 (2000) 1513–1517.
[30] O. Chmaissem, B. Dabrowski, S. Kolesnik, J. Mais, D.E. Brown, R. Kruk, P. Prior, B. Pyles, J.D. Jorgensen, Phys. Rev. B 64 (2001) year.
[31] S. Vyazovkin, A.K. Burnham, J.M. Criado, L.A. Pérez-Maqueda, C. Popescu, N. Sbirrazzuoli, Thermochim. Acta 520 (2011) 1–19.
[32] B. Bulfin, J. Vieten, S. Richter, J.M. Naik, G.R. Patzke, M. Roeb, C. Sattler, A. Steinfeld, Physical chemistry chemical physics 22 (2020) 2466–2474.
[33] B. Bulfin, L. Buttsworth, A. Lidor, A. Steinfeld, Chem. Eng. J. 421 (2021) 127734.
[34] S. Capstick, B. Bulfin, J.M. Naik, M. Gigantino, A. Steinfeld, Chem. Eng. J. 452 (2023) 139289.
[35] R.A. de Souza, Physical chemistry chemical physics 8 (2006) 890–897.
[36] S. Shanmugam, BioImpacts 5 (2015) 55–63.
[37] M. Scheffler (Ed.), Cellular Ceramics: Structure, Manufacturing, Properties and Applications, Wiley-VCH, Weinheim, 2005.
[38] M. Pein, L. Matzel, L. Oliveira, G. Alkan, A. Francke, P. Mechnich, C. Agrafiotis, M. Roeb, C. Sattler, Adv. Energy Mater. 12 (2022) 2102882.
[39] U. Holzwarth, N. Gibson, Nat. Nanotechnol. 6 (2011) 534.
[40] P. Scherrer, Nachrichten von der Gesellschaft der Wissenschaften zu Göttingen, mathematisch-physikalische Klasse, 1918, pp. 98–100.
[41] R.P. Pawar, V. Puri, Ceram. Int. 40 (2014) 10423–10430.
[42] P. Zhao, J. Xu, H. Wang, L. Wang, W. Kong, W. Ren, L. Bian, A. Chang, J. Appl. Phys. 116 (2014) 194901.
[43] A. Leriche, S. Hampshire, F. Cambier, Encyclopedia of Materials: Technical Ceramics and Glasses, Elsevier, 2021, pp. 349–366.
[44] J. Li, F.L. Deepak, Chem. Rev. 122 (2022) 16911–16982.
[45] A.R. Studart, U.T. Gonzenbach, E. Tervoort, L.J. Gauckler, J. Am. Ceram. Soc. 89 (2006) 1771–1789.
[46] U. Betke, K. Schelm, A. Rodak, M. Scheffler, Material 13 (2020) 2437.
[47] H. Ferkel, R. Hellmig, Nanostruct. Mater. 11 (1999) 617–622.
[48] R. Riedel, I.-W. Chen, Ceramics Science and Technology: Volume 1: Structures, 1st edn, Wiley-VCH, Weinheim, 2015.
[49] L. Imponenti, K.J. Albrecht, R. Kharait, M.D. Sanders, G.S. Jackson, Appl. Energy 230 (2018) 1–18.
[50] Q. Yang, Y.S. Lin, Ind. Eng. Chem. Res. 45 (2006) 6302–6310.
[51] S. Kimura, Y. Takagi, S. Tone, T. Otake, J. Chem. Eng. Japan 16 (1983) 217–223.
[52] S. Kimura, AICHE J. 35 (1989) 339–342.
[53] W.D. Kingery, H.K. Bowen, D.R. Uhlmann, Introduction to Ceramics, 2nd edn, Wiley, New York, 1976.